STUDY ON COAL FAILURE MECHANISM AND DEFORMATION EVOLUTION OF COAL UNDER IMPACT

Qi LI[1], Guorui FENG[2], Zhen LI[3*], Zhiwei ZHAI[4], Lingyun ZHANG[5]

In order to analyze the deformation characteristics and mechanical properties of coal under impact load, Brazilian disc splitting test was carried out on coal samples by using split Hopkinson pressure bar and high-speed camera, and the displacement field, strain field and fracture characteristics of coal were quantitatively analyzed. The results show that: (1) the tensile strength of coal under impact load is much higher than the static tensile strength, with an average of 2.02 times; (2) Many physical quantities such as the length, area, degree and fractal dimension of cracks indicate that the crack propagation is nonlinear, and the crack propagation speed reaches hundreds of meters per second, while the propagation speed of different cracks is obviously different; (3) Under the impact, there is a significant difference between the lateral displacement and the longitudinal displacement of coal. The lateral displacement increases rapidly at the initial stage and slowly after the peak. The longitudinal displacement is lower than the lateral displacement at the initial stage of loading, but increases sharply after the middle stage of loading. (4) Impact leads to tensile stress perpendicular to the impact direction, and primary cracks and high-density minerals have obvious influence on the distribution characteristics of compressive strain and tensile strain.

Keywords: dynamic tensile strength; Split Hopkinson Pressure Bar (SHPB); Deformation field; Displacement field

1. Introduction

The average mining depth of coal mine in China is increasing year by year, and dynamic disasters such as rockburst have become research hotspots, and the dynamic tensile strength of coal and rock has attracted widespread attention [1,2]. Limited by the testing principle and experimental conditions, it is difficult to directly test the tensile mechanics of coal. Because of the complex internal structure of coal and the loading rate effect, the mechanical properties of coal under impact are different from those under static load. After years of development and extensive

[1] Department of Mining Engineering, Shanxi Institute of Energy, Jinzhong, Shanxi, China
[2] Department of Mining Engineering, Shanxi Institute of Energy, Jinzhong, Shanxi, China; College of Mining Engineering, Taiyuan University of Technology, Taiyuan, Shanxi, China
[3] *College of Safety and Emergency Management Engineering, Taiyuan University of Technology, Taiyuan, Shanxi, China, email: lizhen@tyut.edu.cn (corresponding author)
[4] Department of Mining Engineering, Shanxi Institute of Energy, Jinzhong, Shanxi, China
[5] Department of Mining Engineering, Shanxi Institute of Energy, Jinzhong, Shanxi, China

application and improvement by researchers, Hopkinson pressure bar has become one of the most extensive methods to study the dynamic mechanical parameters of solid materials [3,4].

Rusinek et al. [5] studied the influence of frictional force at the interface between the sample and the bar on the material response results and believed that the geometry and boundary conditions of the sample had a significant impact on the accuracy of the Split Hopkinson Pressure Bar (SHPB) test results. Kong et al. [6] revealed the influence of axial static load, confining pressure, gas pressure, and impact load on the dynamic mechanical properties of gas containing coal and established verified dynamic constitutive equations. Sun et al. [7] used SHPB to analyses the mechanical behavior and energy dissipation of coal impact loading. Gao et al. [8] investigates the mechanical response and seepage behavior of gas-bearing coal with varying bedding angles under impact loading, revealing that peak strength, dynamic elastic modulus, energy dissipation ratio, and fragment size exhibit non-monotonic trends with increasing bedding angle. Gong et al. [9] revealed the influence of water content and impact load on the dynamic fracture behavior of coal through SHPB experiments. It was found that saturated water coal samples are prone to cracking but slow to propagate, and there is a load threshold effect on their fracture toughness and energy absorption. Feng et al. [10] used SHPB dynamic loading combined with high-speed camera and image processing technology to analyze the influence of water splitting and absorption on the fracture behavior of coal samples, revealing the dynamic mechanical response and damage evolution mechanism of coal rock under different environmental conditions.

The combination of SHPB with other detection methods has also made new progress, such as digital image correlation (DIC), digital volume correlation (DVC) combined with X-ray computed tomography (CT), potential monitoring, etc., to achieve high-precision capture of surface/internal strain fields, crack initiation propagation paths, and damage thresholds of coal and rock during loading, emphasizing the correlation between microscale dynamic response and macroscopic failure. Some studies have proposed precursor criteria [11-14]. Liu et al. [15] innovatively revealed the dynamic failure mechanism of soft coal through a self-developed three-axis loading impact experimental system. By combining SHPB with high-speed optical observation technology or image analysis technology, it is possible to visualize the failure process and study the dynamic evolution mechanism of cracks [16-18]. Mishra [19] and Kumar [20] combined experiments and theory to construct a continuous damage model considering damage plastic coupling.

This study conducts dynamic Brazilian splitting tests on coal samples to analyze their dynamic tensile strength. Using high-speed cameras to record the process of sample damage, analyzing the evolution characteristics of sample displacement and deformation fields through digital image correlation method, and

combining with the fractal box dimension of fractures to study the evolution characteristics of fractures, summarizing the failure law of coal under dynamic load conditions.

2. Experimental Setup and Methodology

2.1 Test System

The experimental setup consists of a Φ50 mm SHPB system integrated with a high-speed imaging system, as shown in Fig. 1. Compressed nitrogen gas propels a 300 mm-long bullet toward the incident bar, generating stress waves. The incident and transmission bars are fabricated from high-strength tungsten steel (elastic modulus: 211 GPa, diameter: 50 mm). Strain gauges (Gauge 1 and Gauge 2) are mounted on the incident and transmission bars, respectively, to capture incident, reflected, and transmitted wave signals. A pair of photoelectric sensors triggers the high-speed camera upon bullet launch, ensuring synchronization between mechanical loading and image acquisition.

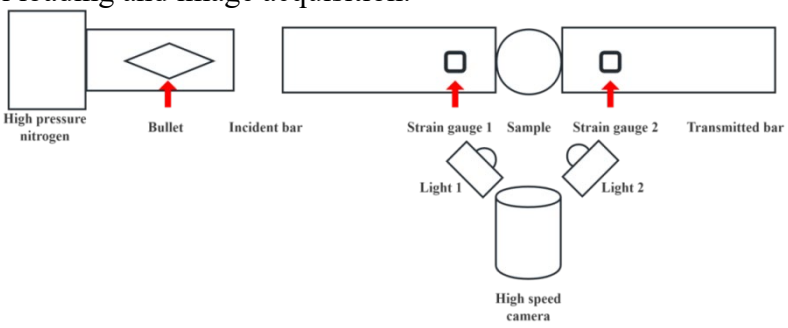

Fig. 1. Schematic diagram of the experimental system

A high-speed camera records the failure process at 84,000 frames per second (fps), with a resolution of 512 × 496 pixels and a time interval of 12 μs between frames. The recorded images were processed using DIC, a non-contact optical technique that tracks pixel-level displacements by comparing successive images, enabling the reconstruction of full-field displacement and strain maps. To ensure the accuracy of DIC, a calibration procedure was performed prior to test using a reference target with known features. The spatial resolution of the imaging system was calibrated to 0.05 mm/pixel based on the specimen size and camera field of view. It is confirmed that the DIC system achieved sub-pixel accuracy (<0.1 pixel).

2.2 Specimen Preparation

Coal samples were collected from the No. 3 coal seam of the West Shaft at Sihe Coal Mine, Jincheng, Shanxi Province [21]. The seam has an average thickness

of 6.45 m, a density of 1.46 t/m³, an elastic modulus of 3.22 GPa, and a Poisson's ratio of 0.28. Twelve specimens were machined from a single coal block to minimize variability. Cylindrical disc specimens with dimensions of Φ50 mm × 25 mm were prepared according to international standards for dynamic Brazilian testing [22]. The end surfaces were polished to ensure flatness within 0.05 mm, and specimens were visually inspected to exclude those with visible microcracks or bedding plane defects. All tests were conducted under controlled conditions at a temperature of 20 ℃ and relative humidity of 50±5%, to minimize environmental variability.

2.3 Test Principle and Data Processing

The experiment was based on one-dimensional stress wave theory. By recording the incident, reflected, and transmitted wave signals via oscilloscope, key mechanical parameters such as stress and strain during loading can be derived. Under the assumption of dynamic force equilibrium at both ends of the specimen, the average strain rate, stress, and strain of the specimen can be calculated using the following equations [23]:

$$\varepsilon = \frac{v}{l}[\varepsilon_{\mathrm{i}}(t) - \varepsilon_{\mathrm{r}}(t) - \varepsilon_{\mathrm{t}}(t)] \tag{1}$$

Force at the incident end of the specimen:

$$P_1 = \mathrm{EA}[\varepsilon_i(t) + \varepsilon_r(t)] \tag{2}$$

Force at the transmission end:

$$P_2 = \mathrm{EA}\varepsilon_{\mathrm{t}}(t) \tag{3}$$

Average stress in the specimen:

$$\sigma = \frac{\mathrm{EA}}{2\mathrm{A_S}}[\varepsilon_{\mathrm{i}}(t) + \varepsilon_{\mathrm{r}}(t) + \varepsilon_{\mathrm{t}}(t)] \tag{4}$$

where ε_i, ε_r and ε_t represent the strain signals from the incident, reflected, and transmitted waves, respectively; v, E and A denote longitudinal wave propagation speed, the elastic modulus and cross-sectional area of the incident bar; l and $\mathrm{A_s}$ are the length and cross-sectional area of the specimen.

Given that the specimen diameter is significantly smaller than the length of the input bar, the average stress at the specimen ends can reasonably approximate the internal stress distribution. Thus, the dynamic tensile strength σ for a Brazilian disc is given by:

$$\sigma = \frac{P_1+P_2}{\pi\varphi\delta} = \frac{\varepsilon\varphi}{\pi\delta}[\varepsilon_1(t) + \varepsilon_r(t) + \varepsilon_t(t)] \tag{5}$$

where φ is the specimen diameter, and δ is the specimen thickness.

The oscilloscope records time-voltage curves from the strain gauges on the incident and transmission bars. These data are imported into MATLAB for processing to obtain stress, strain, and other derived parameters.

3. Results and discussion

3.1 Dynamic tensile strength

Since voltage is proportional to strain rate, strain values are obtained by integrating the recorded strain rate data. Combined with the calculated stress, the stress–strain curve for each specimen is constructed. Fig. 2 is a typical stress–strain curve.

As shown in Fig. 2, the maximum tensile strength of Sample 1 reaches 4.0075 MPa at a strain value of 9.11×10^{-3}. Prior to reaching this strain, the dynamic tensile strength increases proportionally with strain, though the rate of increase gradually diminishes. In the latter half of loading, the strength decreases rapidly until specimen failure occurs. The trend of dynamic tensile strength variation resembles that observed under static loading, but the magnitude is significantly higher. The measured dynamic tensile strengths of the tested specimens range from 3.84 to 4.87 MPa, averaging 2.02 times the static tensile strength. Given that the bullet velocity was kept constant across tests, variations in strength are attributed to inherent heterogeneity among the specimens.

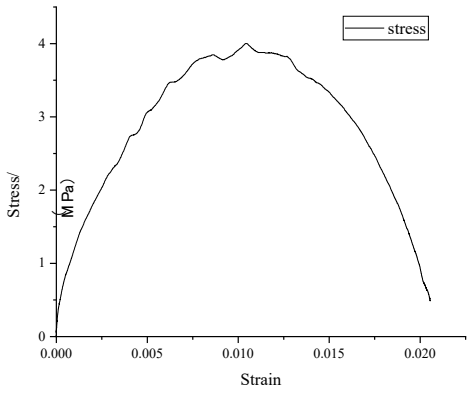

Fig. 2. Typical stress–strain curve of a coal specimen under dynamic loading

The dynamic and static tensile strength of coal samples can be seen in Table 1. The average dynamic tensile strength is 4.36 MPa, ranging from 3.84 to 4.87 MPa, approximately 2.02 times the average static tensile strength of 2.16 MPa. The higher dynamic strength is attributed to strain-rate sensitivity and the inertial confinement effect during rapid loading.

Table 1

Dynamic and Static Tensile Strengths of Specimens

Specimen	Dynamic Tensile Strength (MPa)	Static Tensile Strength (MPa)
1	4.31	2.31
2	4.64	1.86
3	3.84	2.29
4	4.22	2.35
5	4.87	1.89
6	4.26	2.28
Average	4.36	2.16

Table 2

Statistical Analysis of Dynamic and Static Tensile Strengths

Items	Dynamic Tensile Strength	Static Tensile Strength
CV	8.08%	10.54%
SD	0.358	0.225
Cohen's d	7.358	
Shapiro-Wilk	p=0.285	p=0.451
T-test	Mean diff=2.20 MPa	
	p< 0.001	
	T=9.61	

To validate the change of tensile strength under impact loading, a comprehensive statistical analysis was performed on the data in Table 1. The dynamic tensile strength showed a mean value of 4.36 MPa with a low coefficient of variation (CV=8.08%), suggesting good consistency of the dynamic test results. A paired-sample t-test was conducted and the result showed a statistically significant difference (mean difference=2.20 MPa, $p<0.001$), with a 95% confidence interval of [1.74, 2.66] MPa, indicating that strain rate sensitivity play critical roles. The effect size, measured by Cohen's d, was calculated to be 7.358, which represents a very large practical significance. The low coefficient of variation and normal distribution of data support the reliability of the experimental results.

3.2 Crack propagation characteristics

The evolution of the disc specimen is described as follows:

(1) At the initial stage of impact, no visible changes occur at the specimen ends, although the entire disc undergoes a slight leftward displacement.

(2) In the 12 μs image compared to the initial state, minor longitudinal deformation is observable within the elliptical region in Fig. 3.

(3) By 24 μs, new cracks appear. Cracks labeled a and b in Fig. 3 measure 9.628 mm and 5.792 mm in length, respectively.

(4) At 36 μs, crack a continues to extend, while a new crack c forms on the right side of crack b, eventually connecting to it and propagating through the right boundary of the specimen. Crack a extends to 12.906 mm, crack c measures 7.453 mm, and the angle between b and c is 161.79°.

(5) At 48 μs, a new crack d (12.546 mm long) forms on the left side of crack a, making an acute angle with it. Simultaneously, a new crack e (8.956 mm long) appears at the upper-left tip of crack b, while existing cracks continue to widen.

(6) By 60 μs, the primary crack fully traverses the specimen, connecting with crack e. A new crack nearly parallel to the main fracture emerges above it.

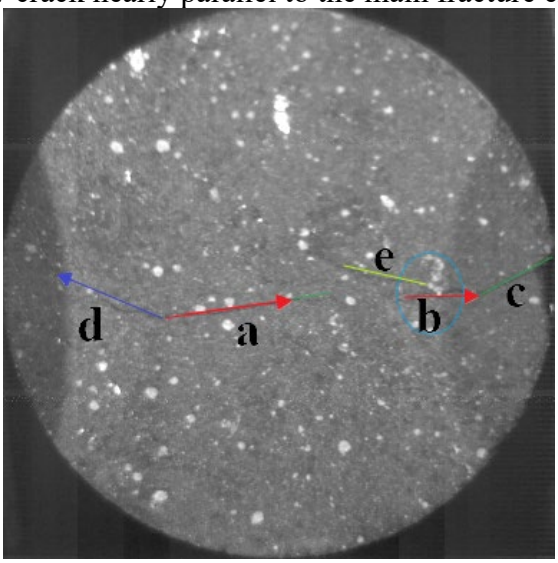

Fig. 3. Schematic diagram of fracture expansion

All images were calibrated using a consistent scale to determine the number of pixels per unit length. In order to highlight the detail changes, all images are selected region of interest(ROI) with fixed position to conduct comparative analysis, as shown in Figure 4.

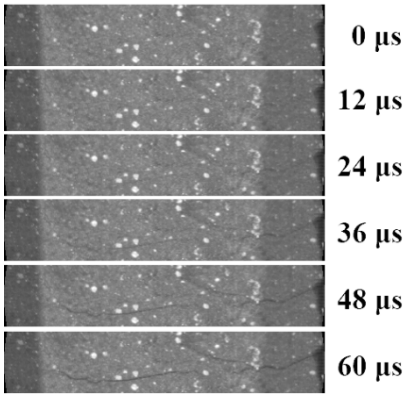

Fig. 4. Comparison of fracture propagation of different frames

According to the crack length and time interval of each sampled image, it is calculated that the crack propagation speed of crack a and crack b is 273.167 m/s and 621.08 m/s respectively. Considering the material distribution (coal, minerals) and stress position near the crack extension, it can be known that: (1) Under the impact, the coal crack extension is very rapid and the difference is huge, and the main influencing factors are the primary internal structure characteristics and stress state. (2) The crack propagation of the sample is mainly along the stress direction, accompanied by derivative cracks with an included angle of about 20 or cracks nearly parallel to it.

3.3 Analysis of crack evolution

The quantitative research on cracks is carried out from two aspects: (1) the scale change in the process of crack expansion, including quantitative indicators such as crack length, crack area and average width; (2) On the basis of Section 3.2, the morphological characteristics in the process of fracture evolution are quantified by the physical quantity of fractal dimension. In this paper, Fiji [24] is used to analyze the image of high-speed camera, and the physical quantities such as threshold segmentation, scale setting, length and area are measured, and the dimension of two-dimensional image box is analyzed.

3.3.1 Evolution of Crack Dimensions

Quantitative research on the size of cracks is carried out, and the intuitive indicators include crack length, crack width and total crack area. Here, two indexes are defined: crack degree and average crack width.

Firstly, the fracture degree is defined as the ratio of the total fracture area to the cross-sectional area of the sample, and the formula is as follows:

$$M_f = A_i / A_s \tag{6}$$

Where M_f is the fracture degree, A_i is the total fracture area, and A_s is the cross-sectional area of the sample.

The second index is the average crack width, that is, the ratio of the total crack area to the crack length.

The above two physical quantities can quantitatively describe the fracture evolution, and a fixed ROI is selected to analyze the images in each stage of the impact process. The analysis results of each physical quantity are shown in Fig. 5.

According to Fig. 5, after the impact, the overall length of the fracture presents two stages of approximate linear growth, and the growth rate is faster before 36 μs, and then the growth rate decreases obviously. The essence of fracture degree is the area ratio, and the histogram shows that the fracture degree is an accelerated growth trend during the whole impact process, which is completely

different from the variation law of fracture length. However, the variation law of crack area and crack length leads to the characteristics that the average crack width changes in two steps and then accelerates.

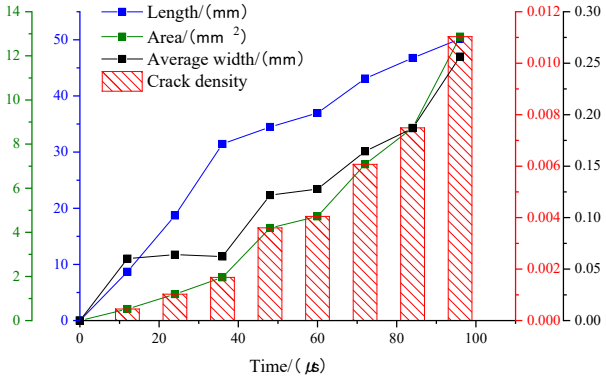

Fig. 5. Variation of crack parameters during impact loading

3.3.2 Evolution of Fractal Dimension

In order to analyze the evolution characteristics of cracks in disk samples, this paper combines image processing and fractal dimension measurement to calculate the fractal dimension D of cracks. The variable D is a parameter describing the degree and complexity of crack propagation, and D is directly proportional to the curvature and complexity of crack propagation. Therefore, it is necessary to process the high-speed camera image of the sample. The treatment process includes: (1) selecting the regions of interest (ROI)； of the sample; (2) improve the image contrast; (3) image threshold segmentation; (4) Image binarization. Calculate and count the box dimension of cracks in each frame image, and the result is shown in Fig. 6.

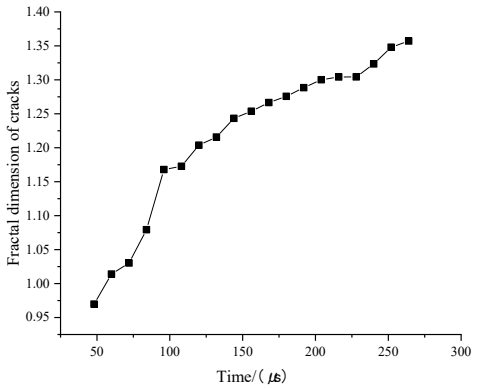

Fig. 6. Relationship between crack fractal dimension and time

The curve indicates that crack system complexity increases over time, rising sharply before 96 μs and then leveling off. Linear and cubic polynomial fitting were applied; the higher goodness-of-fit for the cubic model suggests that crack propagation under dynamic tension is nonlinear and exhibits chaotic characteristics.

3.4 Spatiotemporal Evolution of Displacement and Strain Fields

DIC results show that vertical (tensile) displacement increases rapidly in the mid-to-late stage, exceeding lateral displacement before failure. Vertical strain is predominantly tensile, forming an "X"-shaped pattern at failure, consistent with Brazilian test mechanics.

DIC was used to compare post-impact images with the initial state, enabling reconstruction of 2D displacement and strain fields.

Fig. 7 and 8 show the evolution of displacement fields parallel (u-field) and perpendicular (v-field) to the loading direction, respectively. Fig. 7(a) and 8(a) correspond to a stress level of 0.011 MPa. The stress values are determined based on the frames from the high-speed camera, combined with the stress–strain curve in Fig. 2. At this stage, the u-displacement field shows minimal values, whereas the v-field exhibits clear separation between the upper and lower semicircles, albeit with small magnitudes. Compared to Fig. 7(a), the u-field at 0.203 MPa and 0.655 MPa shows significantly increased displacement, with the smallest values near the left end (transmission side). The v-field maintains its directional pattern but with increasing magnitude.

Fig. 7(d)–7(h) reveal that the low-displacement zone near the incident end persists but rapidly diminishes in extent. In contrast, Fig. 8(d)–8(h) show that the v-field develops a consistent pattern of opposing motion in the two semicircles, with displacement increasing throughout loading. Fig. 7(i) and 8(i), representing post-peak conditions, show a slight overall reduction in u-displacement compared to peak levels, with localized zones of high displacement appearing near cracks. Similarly, the v-displacement field exhibits reduced values in some regions, while crack-proximal areas display localized fluctuations.

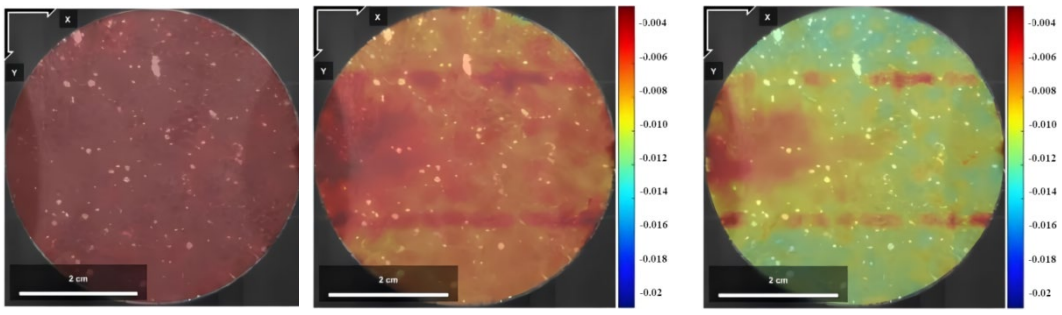

(a)0.011 MPa/0 μs (b)0.203 MPa /12 μs (c)0.655 MPa/24 μs

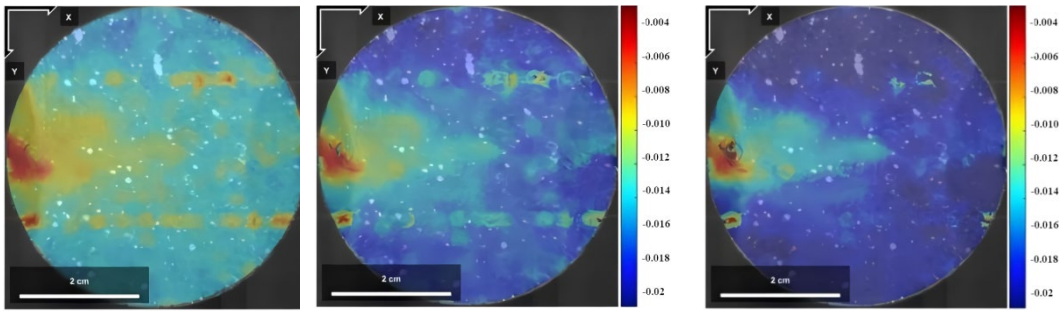

(d)1.330 MPa/36 μs (e)2.090 MPa/48 μs (f)2.776 MPa/60 μs

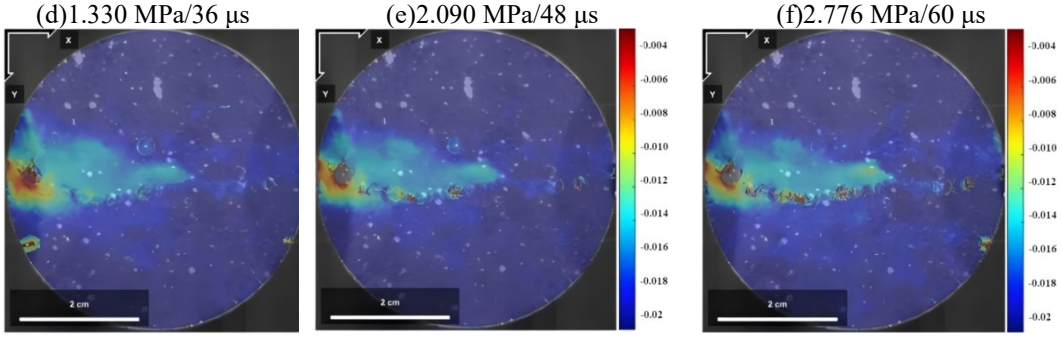

(g)3.476 MPa/72 μs (h)3.833 MPa/84 μs (i)3.651 MPa/96 μs

Fig. 7. Evolution of u-displacement field (horizontal direction)

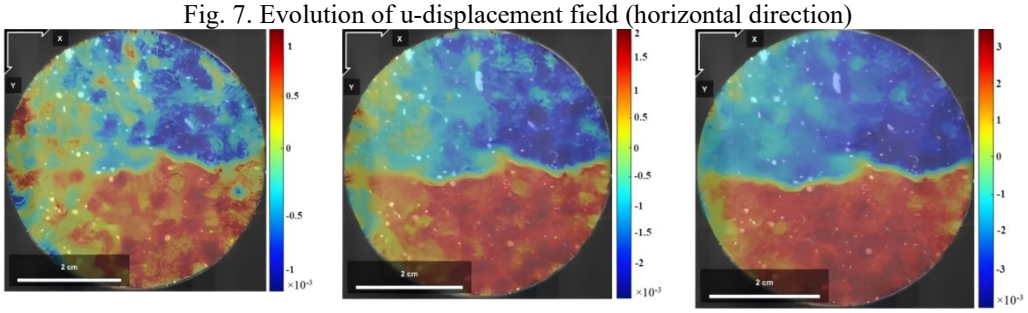

(a)0.011 MPa/0 μs (b)0.203 MPa /12 μs (c)0.655 MPa/24 μs

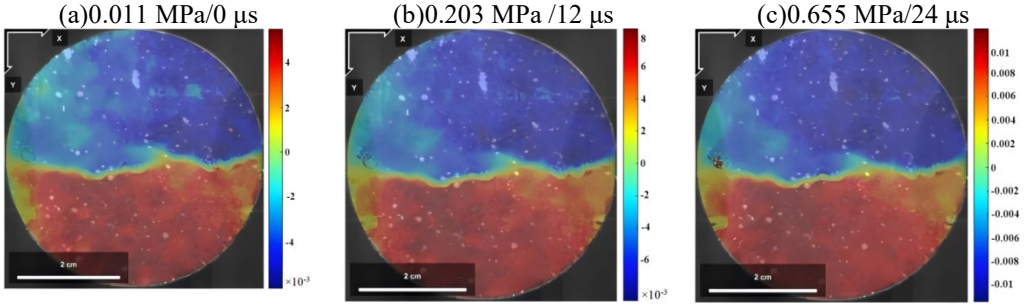

(d)1.330 MPa/36 μs (e)2.090 MPa/48 μs (f)2.776 MPa/60 μs

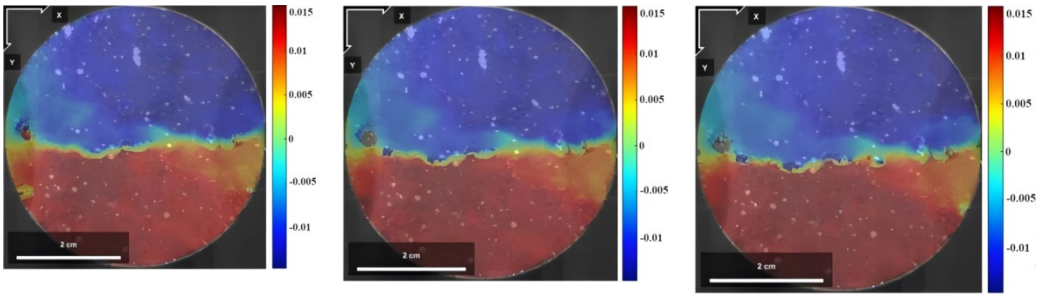

(g)3.476 MPa/72 μs (h)3.833 MPa/84 μs (i)3.651 MPa/96 μs

Fig. 8. Evolution of v-displacement field (vertical direction)

Combining observations from both displacement fields, lateral (u) displacement increases significantly with stress, with localized high-displacement zones attributable to high-density mineral inclusions. The vertical displacement field of coal samples generally takes the loading center line as the dividing line, and the two semicircles move backwards. The vertical displacement shows an accelerated growth trend with the increase of stress. At the initial stage of loading, the vertical displacement field is lower than the horizontal displacement, but before the peak stress, the vertical displacement field quickly exceeds the horizontal displacement, indicating that the vertical displacement increases obviously due to the evolution of cracks.

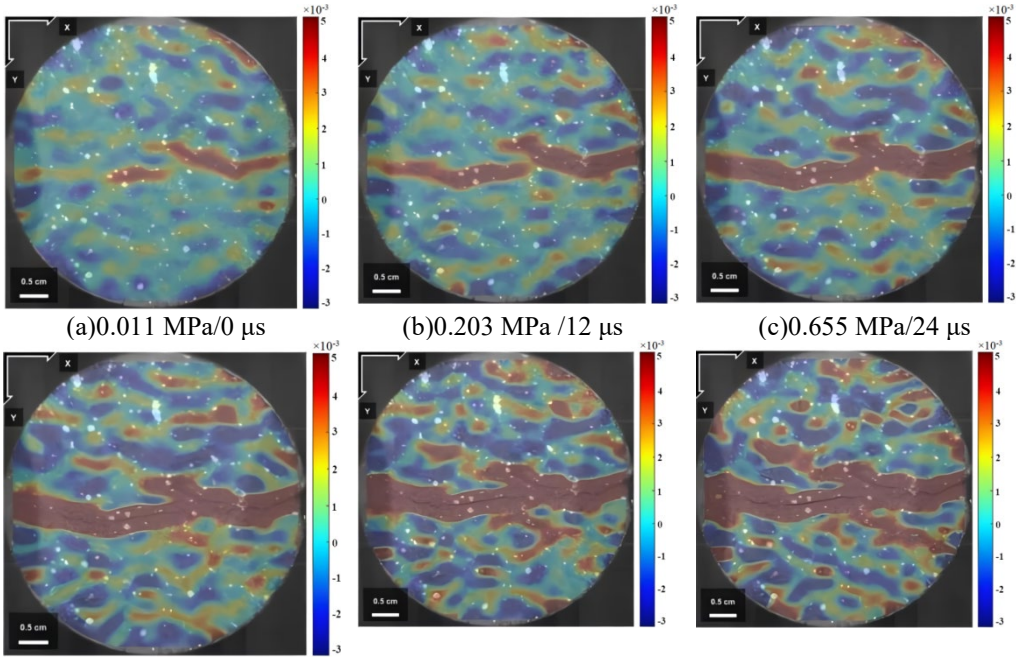

(a)0.011 MPa/0 μs (b)0.203 MPa /12 μs (c)0.655 MPa/24 μs

(d)1.330 MPa/36 μs (e)2.090 MPa/48 μs (f)2.776 MPa/60 μs

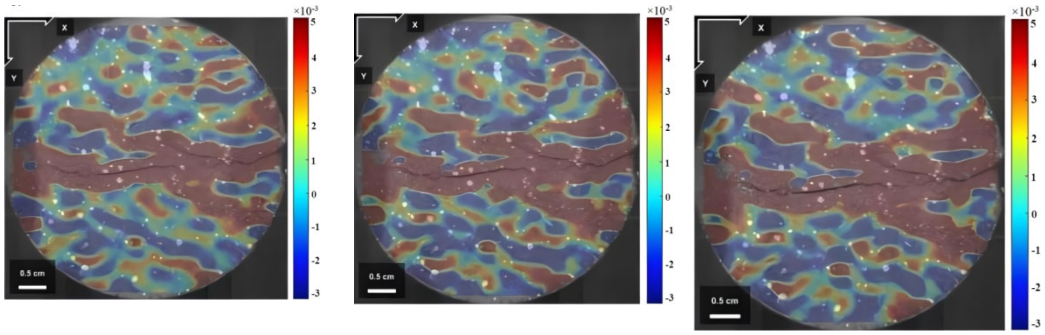

(g)3.476 MPa/72 μs (h)3.833 MPa/84 μs (i)3.651 MPa/96 μs

Fig. 9. Vertical strain contour map of the specimen

The vertical strain contours is shown in Fig. 9. The tensile stress is positive and the compressive stress is negative. It can be seen that under the impact, the tensile strain of the sample first appears in the strip distribution along the central axis of the incident rod, and the area is concentrated in the new crack, and local tensile strain also appears at the edge of the disk. With the impact, the tensile strain area expands rapidly, and the compressive strain in some areas also increases. Subsequently, the tensile strain zone runs through the sample, but the original image of the corresponding stage is observed, and the sample is not completely destroyed. Finally, the sample forms an X-shaped tensile strain region. Generally speaking, the tensile strain region mainly exists in the newly-developed cracks near the central axis, and it presents a point distribution at the edge of the sample and other regions, while the compressive strain region does not appear failure phenomenon. The strain nephogram shows that the failure of the sample is caused by tensile stress perpendicular to the impact load direction.

4. Conclusions

This paper uses split Hopkinson pressure bar to carry out Brazilian splitting test on coal samples, studies the difference between dynamic tensile strength and static tensile strength of coal samples, and analyzes the fracture index, propagation characteristics and temporal and spatial evolution characteristics of displacement field and strain field by Fiji and digital image correlation method, and draws the following main conclusions:

(1) Under the impact load, the dynamic tensile failure of coal samples occurs, and the average dynamic tensile peak strength is 2.02 times of the static tensile strength.

(2) In the process of impact, the crack propagation speed is rapid, but the numerical value is very different, which is caused by the uneven stress caused by the internal structural characteristics of coal and the distribution of different materials.

(3) In the process of impact, the variation characteristics of fracture length and area are different. The fracture length increases linearly with two different slopes, while the fracture degree keeps accelerating. The fractal box dimension of fracture shows that the complexity of fracture increases with the impact, and the fracture propagation is nonlinear and chaotic.

Under the impact load, the lateral displacement of the sample increases obviously at the initial stage, but the growth rate decreases after the peak. However, the variation law of vertical displacement is opposite, and obvious back displacement perpendicular to the central axis appears at the initial stage of impact. The vertical strain is mainly tensile strain distribution, and the tensile strain distribution is mainly point-like at the edge of the sample and other areas.

Acknowledgments

This research was funded by the Young Scholar Program (Category A Continuation Funding) of National Natural Science Foundation of China (Grant No. 52525401), Youth Project of Shanxi Basic Research Program (Grant No. 202303021212292), the National Natural Science Foundation of China (No.52474141), the Fundamental Research Program of Shanxi Province (Grant No.202403021211069, 202103021224333) and the Top Young Talents (in the Field of Technological Innovation) of Shanxi Three Jin Talents Program.

REFERENCES

[1] *W. Wang, B. Zhao, Y. Zhao,* "Effects of bedding orientation and loading rate on fracture behaviors in coal: Analysis of experiments", in Theoretical and Applied Fracture Mechanics, **vol. 139,** 2025, pp. 105012.

[2] *P. Gopinathan, T. Subramani, S. Barbosa, D. Yuvaraj*, "Environmental impact and health risk assessment due to coal mining and utilization", in Environmental Geochemistry and Health, **vol. 45**, no. 10, 2023, pp. 6915 – 6922.

[3] *S. Yang, J. Ning, X. Zhang, J. Wang, X. Shi, X. Qu*, "Determination of critical energy for coal impact fracture under coupled static-dynamic loading", in Eng. Failure Analysis, **vol. 160**, 2024, pp. 108222.

[4] *X. Guan, X. Hou, J. Sun, Y. Liu*, "Investigating the dynamic behavior and tensile properties of coal gangue shotcrete under impact loading conditions SHPB device", in Journal of Building Eng., **vol. 98,** 2024, pp. 111060.

[5] *A. Rusinek, T. Jankowiak, A. Bendarma*, "Improving Dynamic Material Characterization in SHPB Tests Through Optimized Friction Correction", in Materials, **vol. 18**, no. 18, 2025, pp. 4327.

[6] *X. Kong, S. Li, E. Wang, P. Ji, X. Wang, H. Shuang, Y. Zhou*, "Dynamics behaviour of gas-bearing coal subjected to SHPB tests", in Composite Structures, **vol. 256**, no. 2021, pp. 113088.

[7] *Z. Sun, Y. Wu, J. Li*, "Mechanical behavior and energy dissipation characteristics of coal under coupled 3D static and graded cyclic impact loading", in Journal of Rock Mechanics and Geotechnical Eng., **vol. 02**, no. 21, 2025.

[8] *L. Gao, H. Zhao, H. Liu*, "Mechanical response mechanism and seepage characteristics of gas-bearing bedding coal under impact loading", in Eng. Fracture Mechanics, **vol. 326**, 2025, pp. 111425.

[9]*S. Gong, L. Zhou, W. Wang, C. Wang*, "Investigation of dynamic fracture behavior and energy dissipation of water-bearing coal under impact load", in Eng. Fracture Mechanics, **vol. 275**, 2022, pp. 108793.

[10]*J. Feng, W. Liu, T. Zhang, Q. Huang, H. Ding, Y. M*a, "Influence of moisture desorption on dynamic mode I fracture behavior and crack propagation of coal: Experimental and theoretical Insights", in Theoretical and Applied Fracture Mechanics, **vol. 139,** 2025, pp. 105063.

[11] *V. Vishal, D. Chandra*, "Mechanical response and strain localization in coal under uniaxial loading, using digital volume correlation on X-ray tomography images", in International Journal of Rock Mechanics and Mining Sciences, **vol. 154**, 2022, pp. 105103.

[12] *N. Shukla, M.K. Mishra*, "Experimental evaluation of failure characteristics of coal using 2D digital image correlation approach", in Arabian Journal of Geosciences, **vol. 13**, no. 20, 2020, pp. 1060.

[13] *N. Shukla, M.K. Mishra*, "Assessment of crack stress thresholds and development of a pre-failure indicator using Digital Image Correlation approach for coal specimen", in Geomechanics and Geophysics for Geo-Energy and Geo-Resources, **vol. 7**, no. 4, 2021, pp. 103.

[14] *F. Robbiano, K. Liu, Q.-B. Zhang, L.F. Orellana*, "Dynamic uniaxial compression testing of veined rocks under high strain rates", in International Journal of Rock Mechanics and Mining Sciences, **vol. 15**3, 2022, pp. 105085.

[15] *H. Liu, F. Li, L. Xu*, "Dynamic response and failure mechanisms of laminated soft coal under impact loads: A comprehensive study", in Soil Dynamics and Earthquake Eng., **vol. 198**, 2025, pp. 109546.

[16] *F. Li, C. Wang, B. Xu, D. Liang, Z. Li, T. Zhang, B. Tian*, "Research on dynamic damage path of multi-layered combined coal mass under impact load", in Physics and Chemistry of the Earth, Parts A/B/C, **vol. 138**, 2025, pp. 103872.

[17] *M. Fourmeau, D. Gomon, R. Vacher, M. Hokka, A. Kane, V.T. Kuokkala*, "Application of DIC Technique for Studies of Kuru Granite Rock under Static and Dynamic Loading", in Procedia Materials Science, **vol. 3**, 2014, pp. 691 – 697.

[18] *S. Kumar, A. Das, G. Tiwari*, "A comparative study on the dynamic loading response of heat-treated soft and medium hard rocks", in Eng. Fracture Mechanics, **vol. 292**, 2023, pp. 109579.

[19] *S. Mishra, T. Chakraborty, V. Matsagar*, "Dynamic Characterization of Himalayan Quartzite using SHPB", in Procedia Eng., **vol. 191**, 2017, pp. 2 – 9.

[20] *S. Kumar, A. Das, G. Tiwari*, "A strain rate enhanced continuum damage model for rocks subjected to dynamic loading", in Soil Dynamics and Earthquake Eng., **vol. 200**, 2026, pp. 109819.

[21]*J. Jia, L. Xiao*, "Research on $CO_2/CH_4/N_2$ competitive adsorption characteristics of anthracite coal from Shanxi Sihe coal mine", in RSC Advances, **vol. 14**, 2024, pp. 3498 – 3512.

[22]ASTM D3967-23, "Standard Test Method for Splitting Tensile Strength of Intact Rock Core Specimens with Flat Loading Platens", 2023.

[23] *E. Radi*, "Dual series solution for the standardizedISRM Brazilian disc test modelled as anadvancing contact problem", in Int. J. Rock. Mech. Min, **vol. 173**, January 2024, pp. 105634.

[24] *J. Schindelin, I. Arganda-Carreras, E. Frise, V. Kaynig, M. Longair, T. Pietzsch, S. Preibisch, C. Rueden, S. Saalfeld, B. Schmid*, "Fiji: an open-source platform for biological-image analysis", in Nature methods, **vol. 9**, no. 7, 2012, pp. 676–682.